

Effects of Cavern Spacing on the Performance and Stability of Gas-Filled Storage Caverns[†]

Edward L. Hoffman
Engineering Mechanics and Material Modeling Department
Sandia National Laboratories
Albuquerque, New Mexico 87185

Abstract

Three-dimensional finite element analyses of gas-filled storage caverns in domal salt were performed to investigate the effects of cavern spacing on surface subsidence, storage loss, and cavern stability. The finite element model used for this study models a seven cavern storage field with one center cavern and six hexagonally spaced surrounding caverns. Cavern spacing is described in terms of the P/D ratio which is the pillar thickness (the width between two caverns) divided by the cavern diameter. With the stratigraphy and cavern size held constant, simulations were performed for P/D ratios of 6.0, 3.0, 2.0, 1.0, and 0.5. Ten year simulations were performed modeling a constant 400 psi gas pressure applied to the cavern lining. The calculations were performed using **JAC3D**, a three dimensional finite element analysis code for nonlinear quasistatic solids. For the range of P/D ratios studied, cavern deformation and storage volume were relatively insensitive to P/D ratio, while subsidence volume increased with increasing P/D ratio. A stability criterion which describes stability in terms of a limiting creep strain was used to investigate cavern stability. The stability criterion indicated that through-pillar instability was possible for the cases of $P/D = 0.5$ and 1.0 .

[†] This work, conducted at Sandia National Laboratories, was supported by the U. S. Department of Energy under Contract No. DE-AC04-76DP00789, and was also supported by Tejas Power Corporation.

Contents

Figures	6
Tables	7
1 Introduction	9
2 Problem Description	9
2.1 Cavern Geometry	9
2.2 Structural Model	10
2.3 Thermal Model	13
2.4 Constitutive Models and Material Properties	13
2.5 Stability Criterion	14
3 Analysis Results	16
3.1 Cavern Deformation	16
3.2 Storage Loss	16
3.3 Subsidence	23
3.4 Cavern Stability	25
4 Conclusions	30
5 References	31
Distribution	32

Figures

1	Typical cavern layout.	9
2	Stratigraphy used in variable spacing calculations (not to scale).	10
3	Finite element model of a 7 cavern array for P/D ratios of 6.0, 3.0, 2.0, 1.0, 0.5.	11
4	Single cavern models of (a) a 200 ft-diameter cavern, and (b) a 529 ft-diameter cavern of equal volume to the seven cavern array.	12
5	Schematic of quasi-static stress-strain curve (taken from [2]).	15
6	Final deformed cavern shapes (t = 10 years) for P/D ratios of 6.0, 3.0, 2.0, 1.0, and 0.5.	17
7	Displacement vector plots at 10 years for P/D = 3.0.	18
8	Effective (von Mises) stress distribution at 0.5 years for P/D = ∞, 6.0, 3.0, and 2.0.	19
9	Effective (von Mises) stress distribution at 0.5 years for P/D = 1.0, 0.5, and 0.0.	20
10	Normalized storage volume at 10 years versus P/D for center cavern, surrounding caverns, total facility, and a single cavern of equal volume for (a) a scale of 0 to 1, and (b) magnified scale. Storage volume is normalized to the original cavern volume.	21
11	Vector plot of displacement (t=10 years) near the surrounding caverns for P/D = 0.5. Horizontal cross section taken 500 ft above cavern floor.	22
12	Normalized storage volume as a function of time for P/D ratios of 6.0, 3.0, 2.0, 1.0, and 0.5.	23
13	Magnified (1000 x) subsidence plot of caprock and overburden layers at 10 years.	24
14	Subsidence profiles at 10 years for P/D = 6.0, 3.0, 2.0, 1.0, and 0.5 and for a single cavern of equivalent volume (P/D = 0.0).	24
15	Subsidence over center cavern at 10 years as a function of P/D.	26
16	Subsidence volume at 10 years versus P/D. Subsidence volume is normalized by the original storage volume of the seven cavern array.	26
17	Creep rupture stability criterion (Equation (6)) for P/D = 6.0 and 3.0 at 10 years. Horizontal cross section taken approximately 500 ft from cavern floor.	27
18	Creep rupture stability criterion (Equation (6)) for P/D = 2.0, 1.0, and 0.5 at 10 years. Horizontal cross section taken approximately 500 ft from cavern floor.	28
19	Stability function versus time for P/D = 3.0, 2.0, 1.0, and 0.5.	29

Tables

1 Structural Properties of Salt, **Caprock**, and Overburden 14

1 Introduction

Many gas distribution companies are utilizing underground caverns leached in domal salt for storage of natural gas. One of the primary concerns in the design of gas storage cavern fields is how close the caverns can be spaced without adversely affecting cavern performance or stability of the surrounding salt. Cavern spacing is usually described in terms of the P/D ratio which is the pillar thickness (the width between two caverns) divided by the cavern diameter. It is desirable to minimize the P/D ratio so that a maximum number of caverns can be placed in a given space of land. Therefore, the effects of reducing the P/D ratio on cavern performance (storage volume and subsidence) and cavern stability must be well understood.

This memo presents a spacing study performed using a three dimensional (3D) model of a gas cavern field. The finite element model is based on a seven cavern array. The structural calculations were performed with **JAC3D** [1] for P/D (pillar/diameter) ratios of 6.0, 3.0, 2.0, 1.0, and 0.5. As part of this investigation, a practical concept of demonstrating stability of rock salt was essential. A stability criterion was used [2] which describes failure in terms of a limiting strain. The theory is based on empirical observations of triaxial creep tests.

In the following section, the finite element model is described. Next, the analysis results are presented in terms of cavern performance and integrity. Finally, the conclusions of the investigation are presented in the last section.

2 Problem Description

2.1 Cavern Geometry

The seven cavern array, shown in Figure 1, consists of a center cavern with six equally spaced surrounding caverns. By assuming that the surrounding ring of six caverns are simultaneously formed and identically loaded, symmetry planes can be invoked for a 30° wedge as shown in Figure 1. The finite element models used for this study include a typical domal stratigraphy of salt, **caprock** and overburden as illustrated in Figure 2. The overburden and **caprock** are assumed to be 760 ft and 295 ft-thick, respectively. The cavern geometry chosen for the study is a 1600 ft-high right circular cylinder with a 200 ft diameter. The cavern ceiling is 2500 ft deep or 1445 ft below the **caprock**.

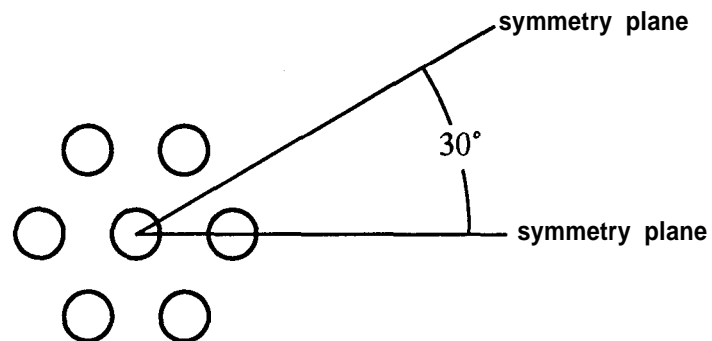


Figure 1. Typical cavern layout.

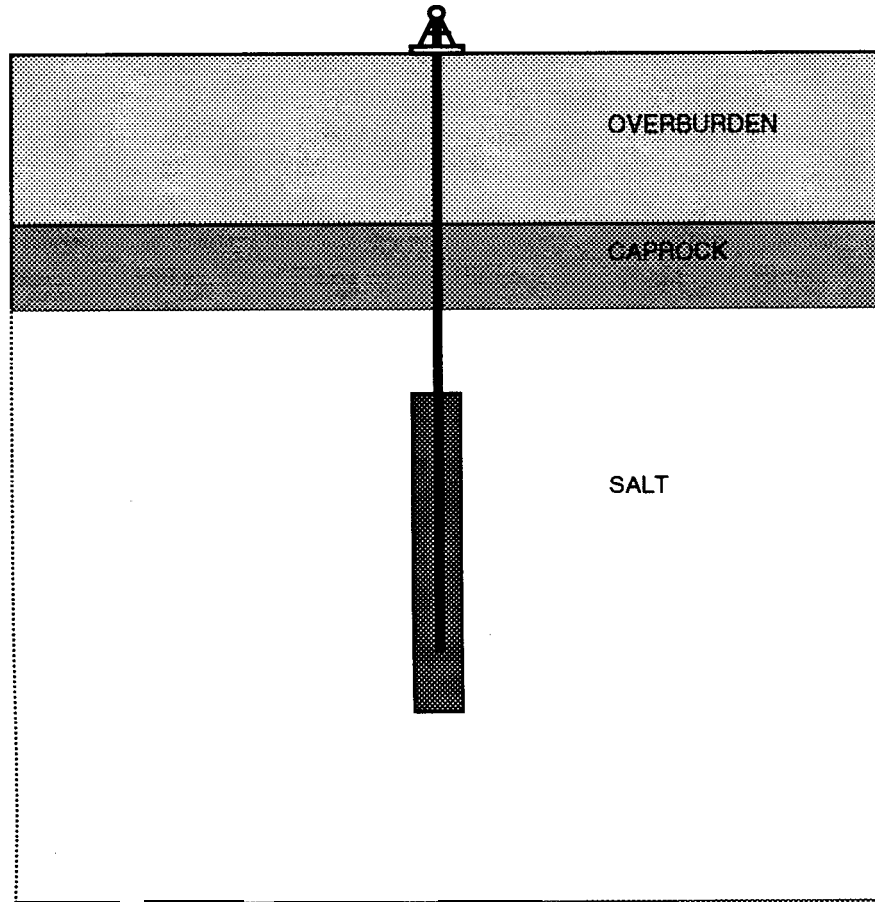


Figure 2. Stratigraphy used in variable spacing calculations (not to scale).

2.2 Structural Model

The 3D finite element model used in the present calculations is shown in Figure 3. The model, constructed of **8-node** bricks, is shown for P/D ratios of 6.0, 3.0, 2.0, 1.0, and 0.5. The $P/D=6.0$ model consists of 23,165 nodes and 18,765 elements, while all others consist of 19,135 nodes and 14,985 elements. Since the number of elements in the pillar is the same for the later four models, the mesh is finer for the smaller P/D ratios as higher stress gradients are expected.

In addition to the above multiple cavern models, two single cavern calculations were performed. The single cavern models are shown in Figure 4. The first is a single cavern of equal size to one of the caverns in the multiple cavern model. The second is a single cavern of equivalent storage volume to the seven cavern model obtained by increasing the cavern diameter ($d_{single}^2 = 7d_{seven}^2$). The first single cavern model represents the case of $P/D = \infty$. The second is approximately equivalent to $P/D = 0.0$. Both models consist of 7,900 nodes and 5,556 elements. Although they are axisymmetric problems, the calculations were performed in 3D for consistency with the multiple cavern calculations.

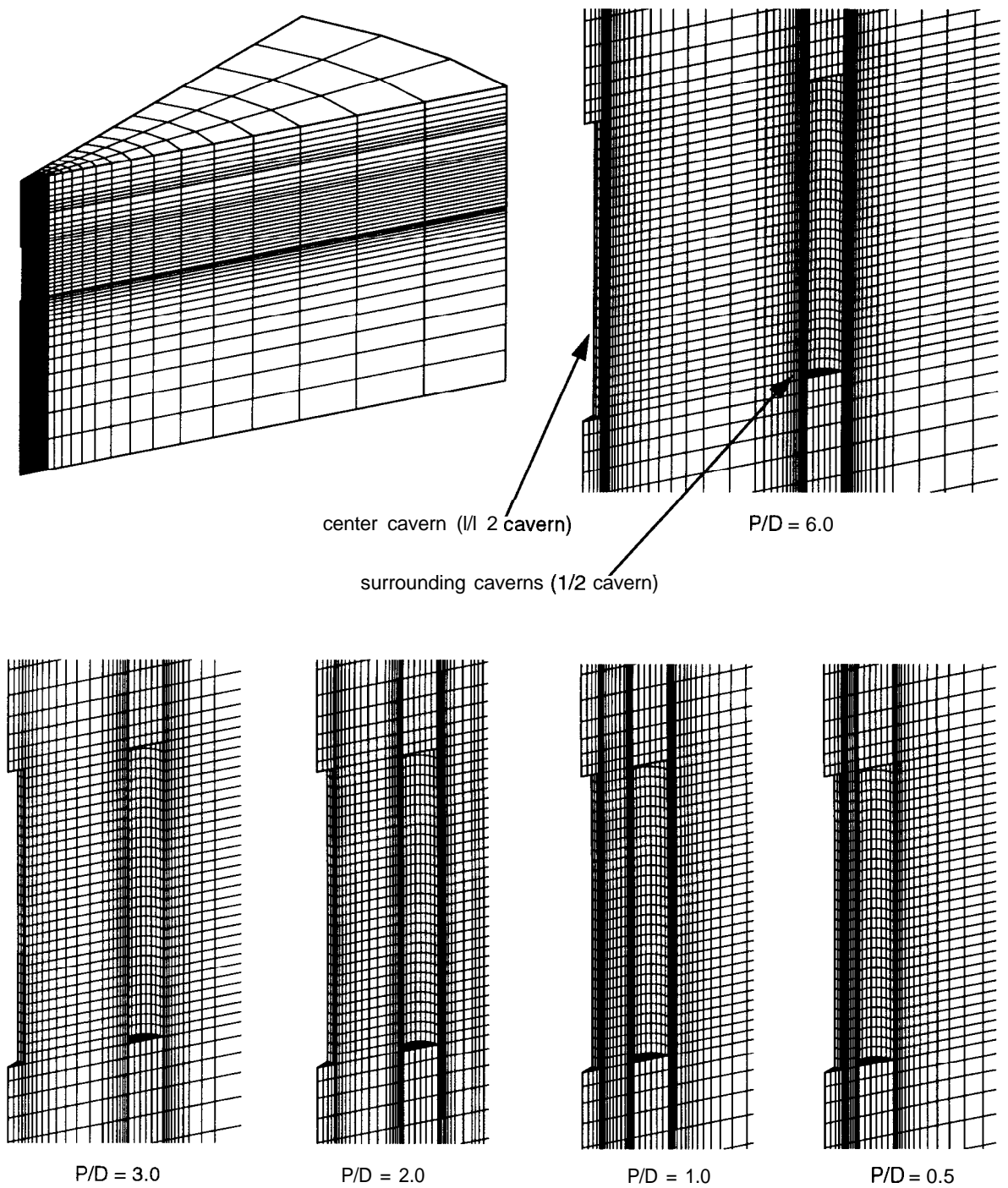


Figure 3. Finite element model of a 7 cavern array for P/D ratios of 6.0, 3.0, 2.0, 1.0, 0.5.

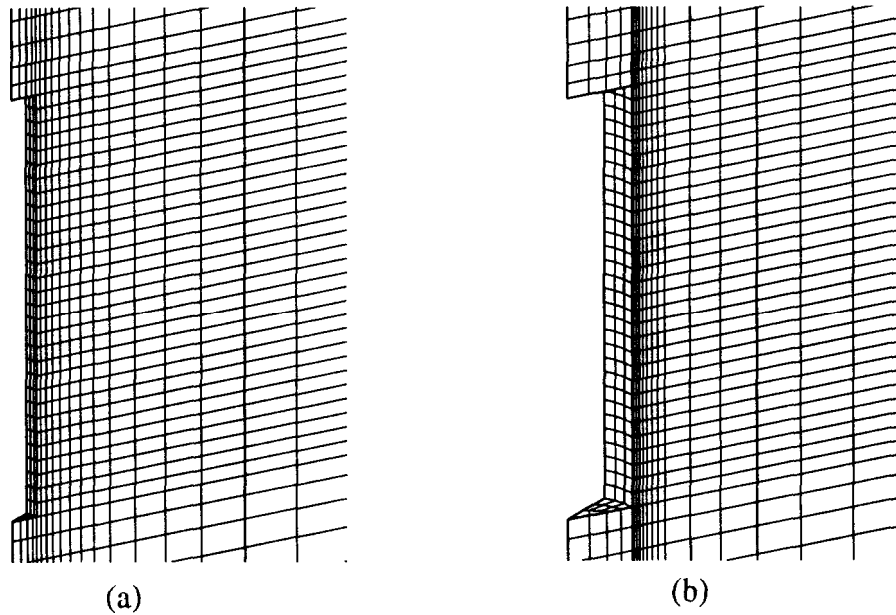


Figure 4. Single cavern models of (a) a 200 ft-diameter cavern, and (b) a 529 ft-diameter cavern of equal volume to the seven cavern array.

The two vertical planar sides of the model represent the symmetry planes illustrated in Figure 1. Displacements were constrained in the direction normal to these planes. The far field boundary (curved boundary) is 3.73 miles (6000 m) from the center cavern, a sufficient distance such that the boundary should not affect the solution. Displacements of the nodes on this boundary were constrained in both horizontal directions. This geometry, an approximation to the actual salt dome stratigraphy, simulates a salt dome of infinite width, while actual salt domes are 1 to 2 miles wide. The affects of a finite dome width will be investigated in future studies. The interface between the salt and caprock was modeled as a frictionless sliding interface. This assumption is appropriate since the actual interface contains many water-filled cavities and relative sliding at this interface has been observed at cavern fields in use.

A uniform pressure distribution is applied to the inside of the caverns to simulate gas storage. The magnitude of the pressure was held constant at 400 psi for the duration of the 10-year simulation (assuming instantaneous cavern formation). This represents a worst case loading since in actual gas storage caverns the storage pressure ranges from 400 to 2000 psi and will be at the lower pressure for a small percentage of the facility service life.

In addition to the pressure loads, gravitational body forces are applied to the rock. Elevation-dependent initial stresses were applied so that the model is at equilibrium at time zero. In the elastic materials (overburden and caprock), the vertical stress component at a given location was applied based on the weight of the material above that point. The horizontal component was applied to be consistent with a vertically loaded elastic material in equilibrium. Under these load conditions, the resulting ratio of horizontal to vertical stress components is defined as follows:

$$\frac{\sigma_h}{\sigma_v} = \frac{v}{1-v} \quad (1)$$

where v is the Poisson's ratio of the material. For the salt, an initial stress state was assumed in which the vertical and horizontal stress components are equal (lithostatic) to the weight of the overlying material.

2.3 Thermal Model

The finite element model included a depth-dependent temperature gradient which starts at 80° F at the surface and increased at the rate of 0.0 12° F/ft. The temperature distribution is important because the creep response of the salt is temperature dependent. Radial temperature gradients due to cavern cooling were not considered in these calculations. Previous 2D cavern studies have shown the predicted cavern deformation to be insensitive to radial thermal gradients developed by cooling effects of the oil [3]. One-way thermal coupling was assumed by entering the thermal data into the structural calculations. This assumption was appropriate since the deformations were not large enough to significantly affect the thermal analysis.

2.4 Constitutive Models and Material Properties

In this section, properties for the caprock, overburden and more particularly the salt are reported in SI units since this is how they were entered into the analysis and how they are commonly reported in geomechanics literature. The overburden and caprock were modeled as elastic materials using the properties listed in Table 1. The properties were obtained from [4] and were for homogeneous samples. The elastic properties for shale were used for the caprock, and those of sandstone were used for the overburden.

The domal salt exhibits both elastic and creep behavior. The creep constitutive model used for this material considered only secondary creep. The creep strain rate is determined from the effective stress as follows:

$$\dot{\epsilon}^{cr} = A \tilde{\sigma}^n \exp\left(-\frac{Q}{RT}\right) \quad (2)$$

where

$\dot{\epsilon}^{cr}$ is the creep strain rate,

$\tilde{\sigma}$ is the effective or von Mises stress,

T is absolute temperature,

A and n are constants determined from fitting the model to creep data,

Q is the effective activation energy (Cal/mole),

R is the universal gas constant (1.987 cal/mole-K).

The creep constants for salt are given in Table 1 and correspond to parameters for the Waste Isolation Pilot Plant (WIPP) salt [5]. Previous studies have shown that WIPP salt and most

Table 1: Structural Properties of Salt, Caprock, and Overburden

	Elastic Properties			Creep Properties		
Material	Young's Modulus, E_{ref} (GPa)	Poisson's Ratio, ν	Density, ρ (kg/m ³)	A (Pa ^{-4.9} /sec)	n	Activation Energy, Q (kcal/mole)
Salt	31.0	0.25	2300	5.79×10^{-36}	4.9	12.0
Caprock	7.0	0.29	2500	--	--	--
Overburden	0.1	0.33	1874	--	--	--

domal salts of the Strategic Petroleum Reserve (SPR) exhibit similar creep behavior [6, 7]. The Young's modulus for rock salt was reduced by a factor of 12.5 from its laboratory or reference value. This reduction has resulted in good agreement between predicted and measured responses for WIPP excavations [8]. Other studies have observed that the secondary creep model with the empirical modulus ($E_{ref}/12.5$) captured unloading behavior observed in laboratory tests more accurately than the secondary creep model with the reference modulus (E_{ref}) [9]. Consequently, this empirical adjustment appears to model stress redistribution around openings in rock salt better than the reference modulus. However, 2D calculations of SPR caverns have demonstrated that this modulus reduction has a small effect on cavern closure and surface subsidence [3].

2.5 Stability Criterion

The criterion used in the present calculations assumes compressive fracture of rock salt by means of a limiting inelastic strain [2]. The limiting strain is a measure of damage before the rock ruptures. The compressive fracture criterion is based on empirical observations in triaxial compression tests. In this model, the axial strain-to-rupture (e^r) is based on the sum of the instantaneous strain (e^i) and the time-dependent creep strain (e^c) and is defined as follows:

$$e^r = e^i + e^c \leq e^u + \alpha (\bar{\sigma} - \sigma^u) \quad (3)$$

where e^u is the ultimate strain, $\bar{\sigma}$ is the deviatoric stress, and σ^u is the ultimate stress. This relationship is illustrated schematically in Figure 5. Laboratory tests indicated that the post-failure behavior of rock salt may be approximated by a line of slope $1/\alpha$. The parameter α increases (or the slope decreases) with increased confining pressure and temperature. Thus, at higher pressures, the rock salt is capable of withstanding higher creep strains.

The two terms on the right side of Equation 3 are always positive. In a study investigating the stability of salt caverns [2], a conservative estimate of the rupture strain was made by assuming $\alpha = 0$, yielding a lower bound approximation in which $e^r = e^u$. Laboratory compression data were fitted by a second order polynomial to yield the limiting strain which is defined as follows:

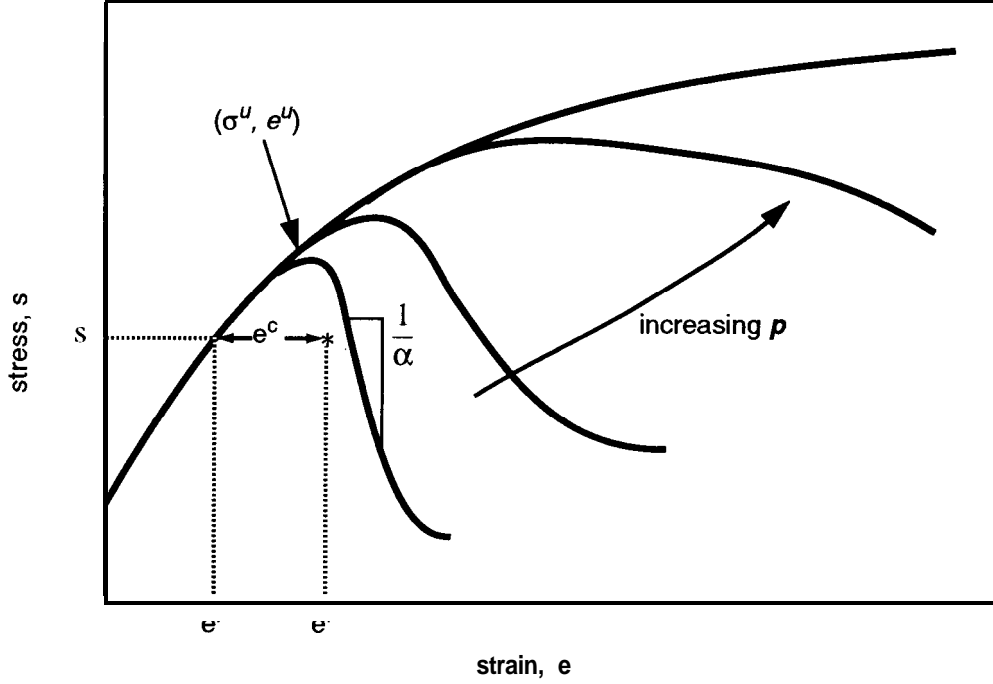


Figure 5. Schematic of quasi-static stress-strain curve (taken from [2]).

$$e^r \approx e^u = 0.155 \text{ for } p > 6 \text{ MPa (870 psi)} \quad (4)$$

$$e^r \approx e^u = c + (a - bp)p \text{ for } p \leq 6 \text{ MPa (870 psi)} \quad (5)$$

where p is pressure, $c = 0.023$, $a = 4.43 \times 10^{-8} \text{ Pa}^{-1}$, and $b = 3.7 \times 10^{-15} \text{ Pa}^{-2}$. Using this definition of strain-to-rupture, a stability function was defined as follows:

$$F = \frac{e^u}{\bar{e}} \quad (6)$$

where \bar{e} is the effective strain. This formulation can be interpreted as a factor of safety in which stability is indicated if $F > 1.0$.

It is important to note that the limiting strain and, therefore, the stability function F are lower bound approximations. The assumption that $a = 0$ implies that at $p = 6 \text{ MPa}$ the salt can withstand no more than 15.5 percent strain. This is contradictory to the behavior illustrated in Figure 5 in which higher pressures yield higher strain limits. Since it is conservative, this theory is best used to predict stability rather than failure. Furthermore, the criterion does not consider the effect of fracture healing.

3 Analysis Results

3.1 Cavern Deformation

The final deformed shapes ($t = 10$ years) of the five cavern spacings are shown in Figure 6. There appears to be little difference between the deformed shapes for $P/D = 6.0$, 3.0 and 2.0 . However, for $P/D = 1.0$ and 0.5 , the surrounding cavern rings appear to be moving in toward the center cavern. This is most extreme for $P/D = 0.5$ in which the surrounding caverns are not closing symmetrically about their centerlines. In particular, the lower part of the cavern (where the creep strains are highest) is moving more than the top.

Figure 7 shows, for the case of $P/D = 3.0$, a vector plot of displacement from (a) a side profile, and (b) a horizontal cross section of the model taken 500 ft from the cavern floor. These plots show the flow path of the creeping salt. The cross section shows that salt flows radially from all sides of both the center and surrounding caverns. This radial flow is fed by vertical flow from above and below the caverns, and by horizontal flow between the surrounding caverns. A “neutral” zone, where the salt is not moving, occurs between the caverns approximately two-thirds the distance from the center cavern and about 500 ft up from the cavern floor. The salt flow from the bottom of the caverns is fed laterally by the horizontal movement of salt.

Contour plots of the von Mises stresses at 0.5 year are shown in Figure 8 for $P/D = \infty$, 6.0 , 3.0 , and 2.0 and Figure 9 for $P/D = 1.0$, 0.5 , and 0.0 . The maximum von Mises stress consistently occurs at the outside edge of the surrounding caverns. For the case of $P/D = \infty$, the stress distribution radiates from the cavern with no interaction with other caverns. For wide cavern spacings ($P/D = 6.0$), stress interactions between caverns occur at the outer fringes of the stress distribution. As the caverns are moved closer together, the interactions occur at even higher stress levels, resulting in higher stresses in the pillar. As the caverns are moved closer together, the stress contours begin looking like that of an individual cavern of equivalent volume ($P/D = 0$).

3.2 Storage Loss

Figure 10 shows the normalized storage volume at 10 years as a function of P/D for the center cavern, surrounding caverns, total storage facility, and for a single cavern with an equivalent volume of a seven cavern array. In each case the storage volume is normalized with respect to the original cavern volume. The plot is shown in two scales. On a scale of 0 to 1, the normalized storage loss appears to be relatively insensitive to cavern spacing. However, slight dependencies are observed in the magnified scale which are not intuitive and require further explanation.

As the P/D ratio is increased, the normalized storage volume of the surrounding caverns decreases, while that of the center cavern increases to a maximum near $P/D = 3.0$, and then decreases. For the total seven cavern storage facility, as the P/D ratio is increased, the storage volume decreases. As the P/D ratio is increased above 3.0 , all three curves converge as the model approaches the case of $P/D = \infty$ (a single cavern). The calculation for the single cavern case yielded a normalized storage volume of 0.643 at 10 years.

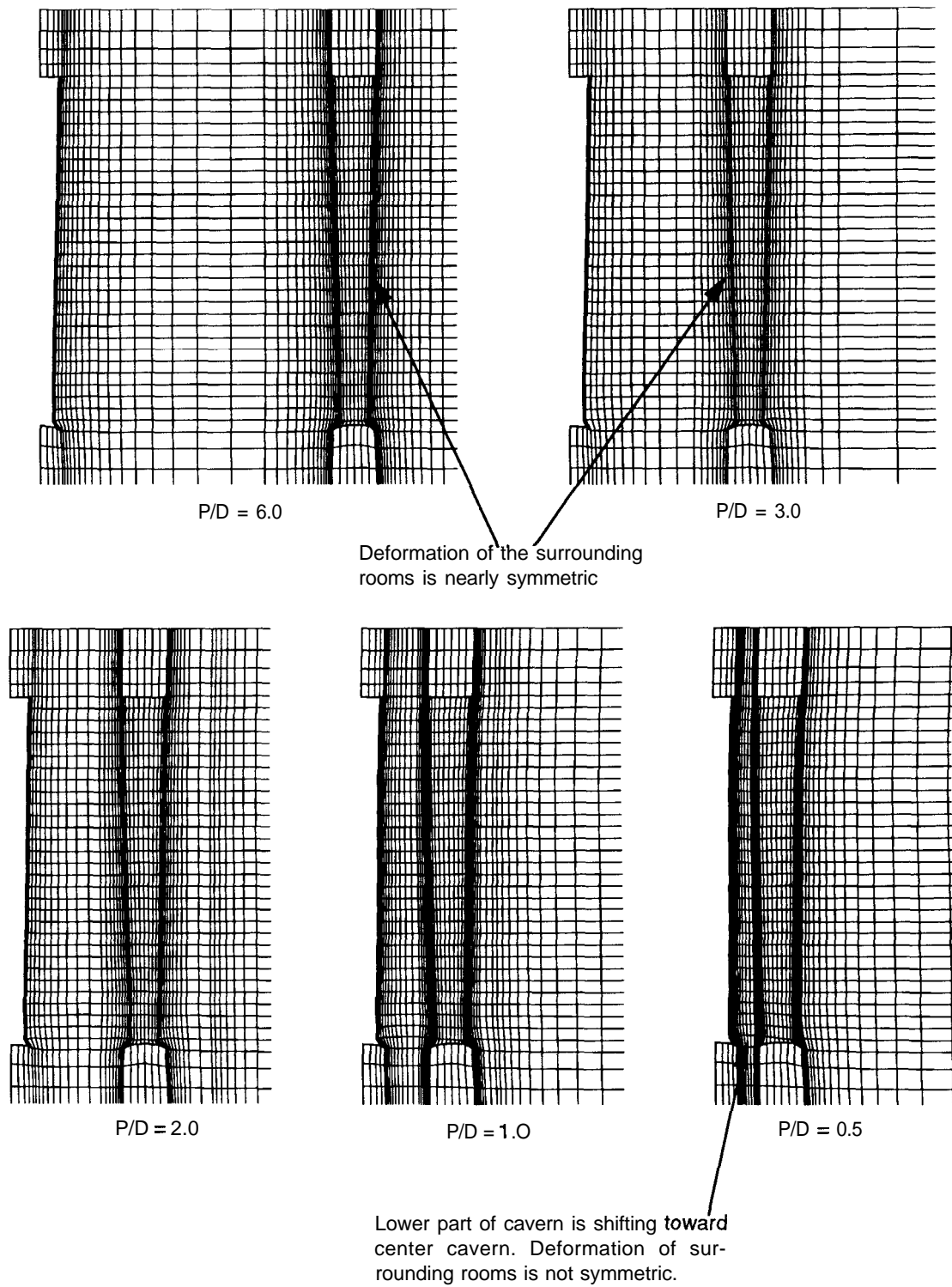


Figure 6. Final deformed cavern shapes ($t = 10$ years) for P/D ratios of 6.0, 3.0, 2.0, 1.0, and 0.5.

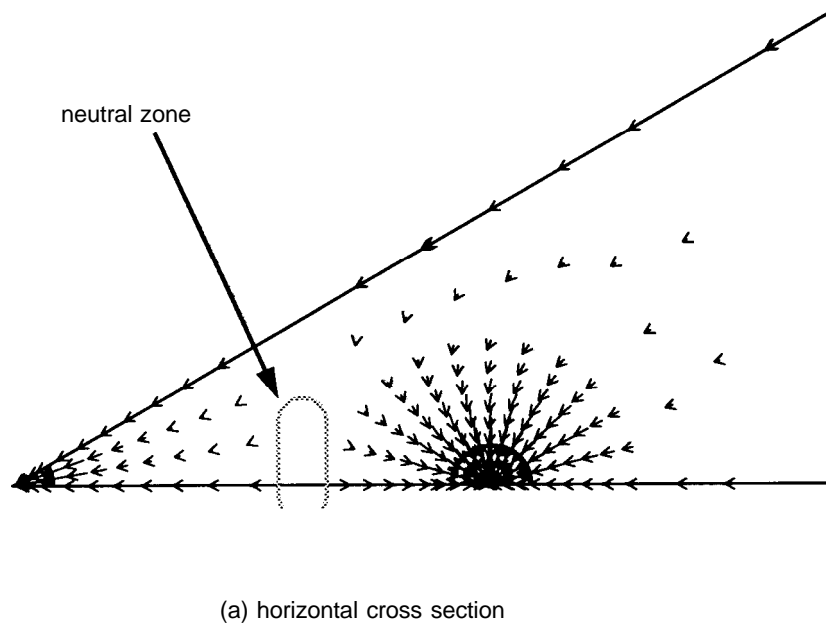
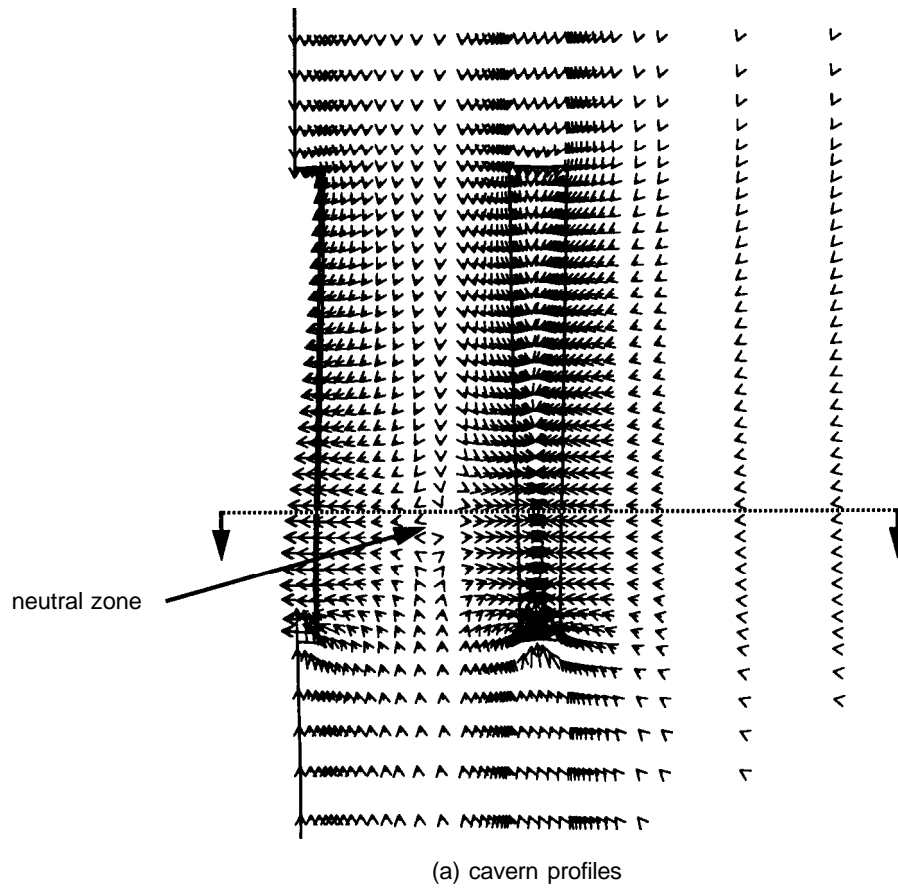


Figure 7. Displacement vector plots at 10 years for $P/D = 3.0$.

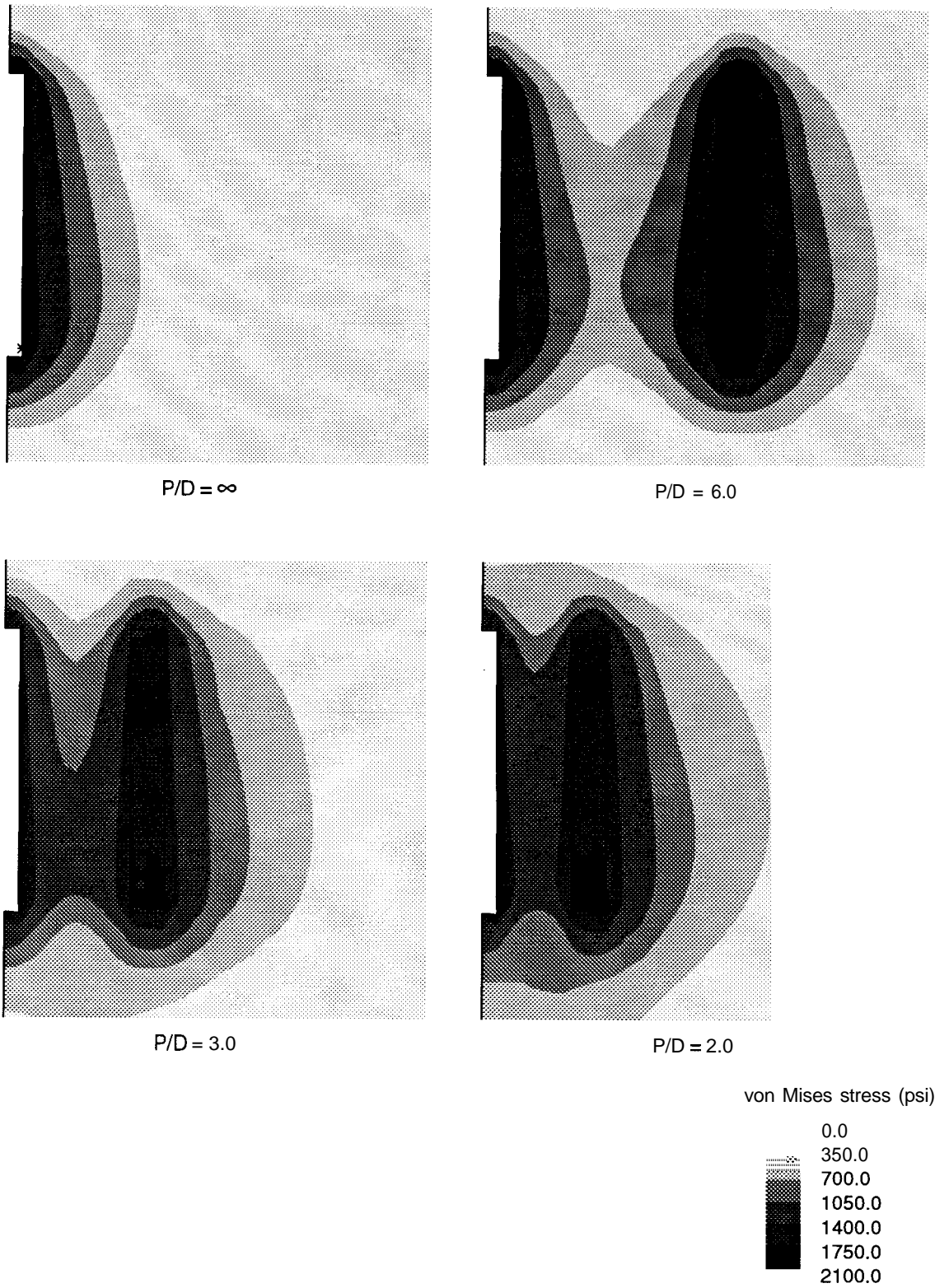
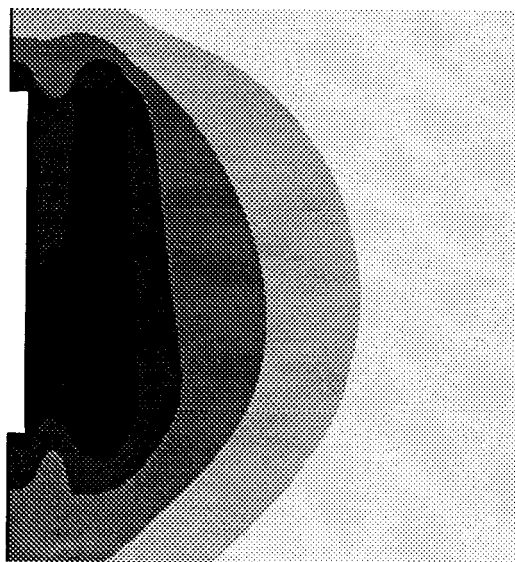
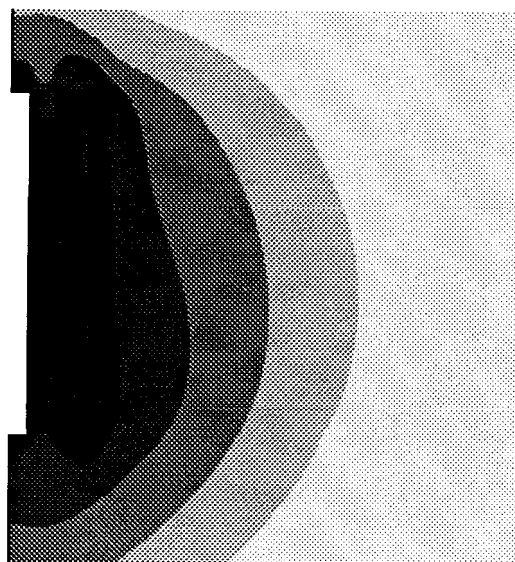


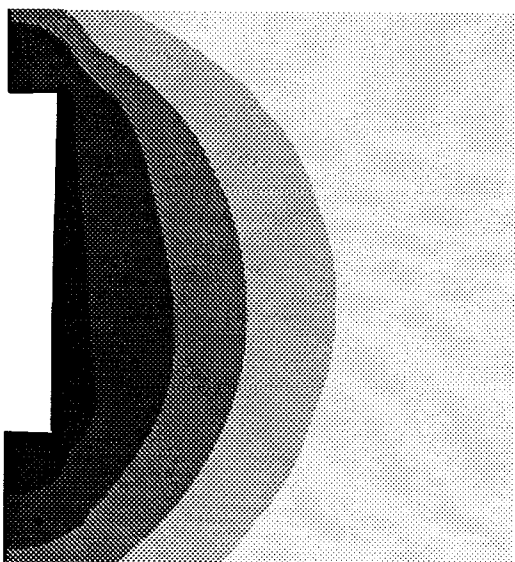
Figure 8. Effective (von Mises) stress distribution at 0.5 years for $P/D = \infty$, 6.0, 3.0, and 2.0.



P/D = 1.0



P/D = 0.5



P/D = 0.0

vonmises stress (psi)

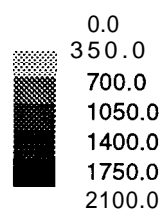


Figure 9. Effective (von Mises) stress distribution at 0.5 years for P/D = 1.0, 0.5, and 0.0.

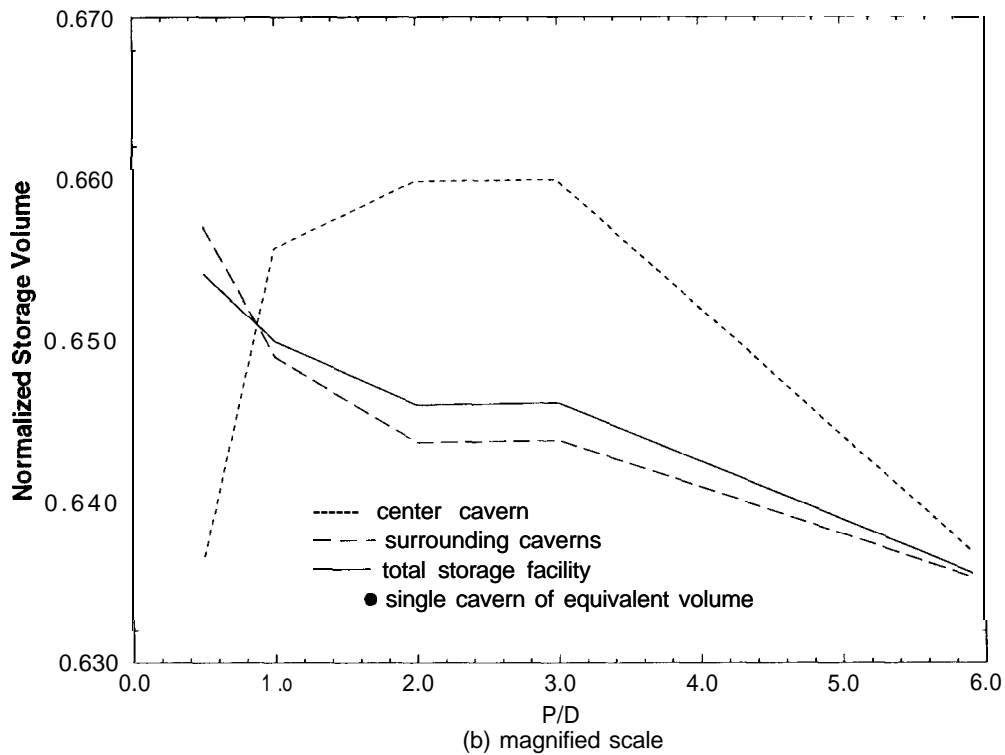
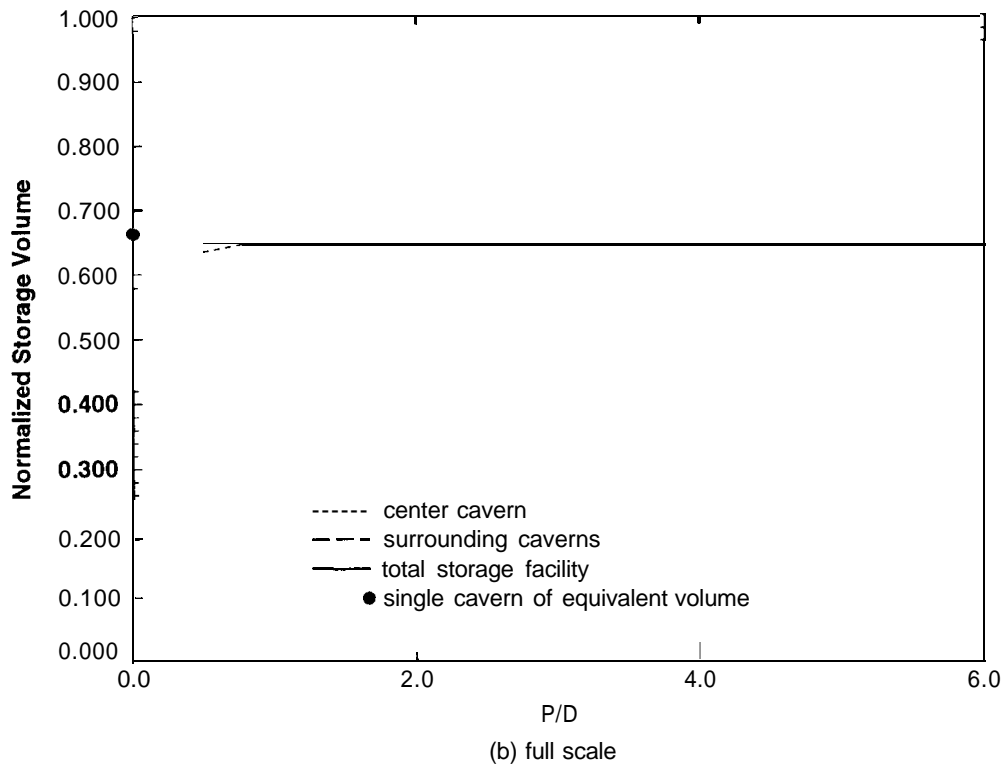


Figure 10. Normalized storage volume at 10 years versus P/D for center cavern, surrounding caverns, total facility, and a single cavern of equal volume for (a) a scale of 0 to 1, and (b) magnified scale. Storage volume is normalized to the original cavern volume.

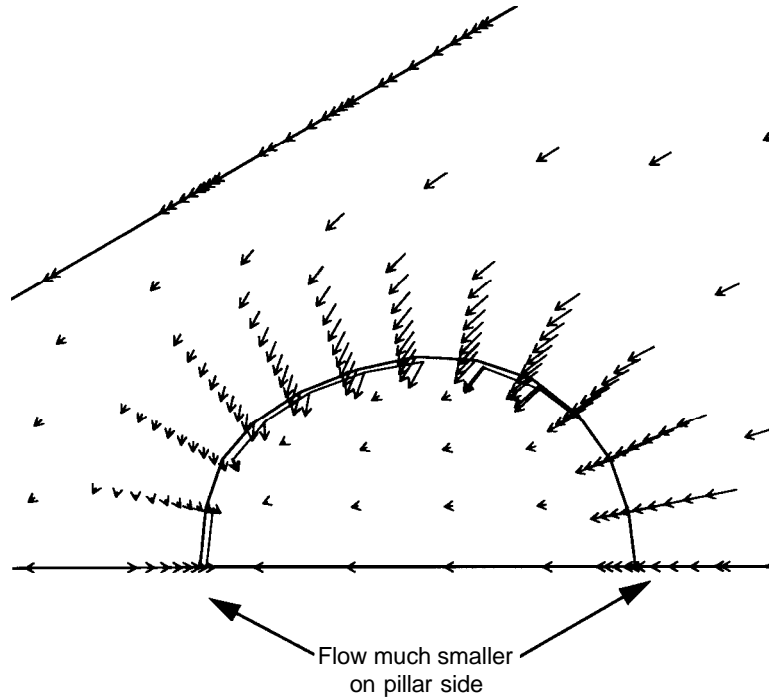


Figure 11. Vector plot of displacement ($t= 10$ years) near the surrounding caverns for $P/D = 0.5$. Horizontal cross section taken 500 ft above cavern floor.

The behavior illustrated in Figure 10 seems counter-intuitive because closer cavern spacing results in smaller pillars which are subject to higher stresses (as seen in Figures 8 and 9) and consequently higher creep rates. Thus, one would expect storage volume to decrease with decreasing P/D ratio. However, there is considerably less salt volume in the pillar available to displace storage volume. Salt behaves according to a deviatoric creep model, thus the creep deformations are a constant volume process. In the case where P/D is large ($P/D > 6$), salt creeps horizontally from all sides of a cavern. In order to get this horizontal movement, the pillar between the caverns must shorten (this behavior is shown in the vector plot in Figure 7). The volume of the pillar is on the order of P^2 , where P is the pillar width between caverns. Thus, the column for $P/D=0.5$ must shorten approximately 16 times that of $P/D=2.0$ in order to yield the same displaced volume. However, the pillar shortens 15 ft for $P/D = 2.0$ and 37 ft for $P/D = 0.5$, only 2.4 times greater. As a result, closure will not be equal on all sides of the surrounding caverns. A vector plot of displacement for $P/D = 0.5$ is shown in Figure 11 for a horizontal cross section 500 ft from the cavern floor. The figure shows salt flow in the vicinity of the surrounding cavern. In contrast to the same plot in Figure 7 for $P/D=3.0$, there is much more radial salt flow from the right side than from the pillar. This nonsymmetrical closure is also observed in Figure 6 for the case of $P/D = 0.5$. For smaller P/D ratios the pillar moves toward the center cavern, resulting in more closure of the center cavern and less closure of the surrounding caverns. Note that the closure becomes more symmetrical as the P/D ratio is increased. Hence, closer cavern spacing yields less storage loss (in a given time period) because there is less salt mass available in the pillars to displace the storage volume.

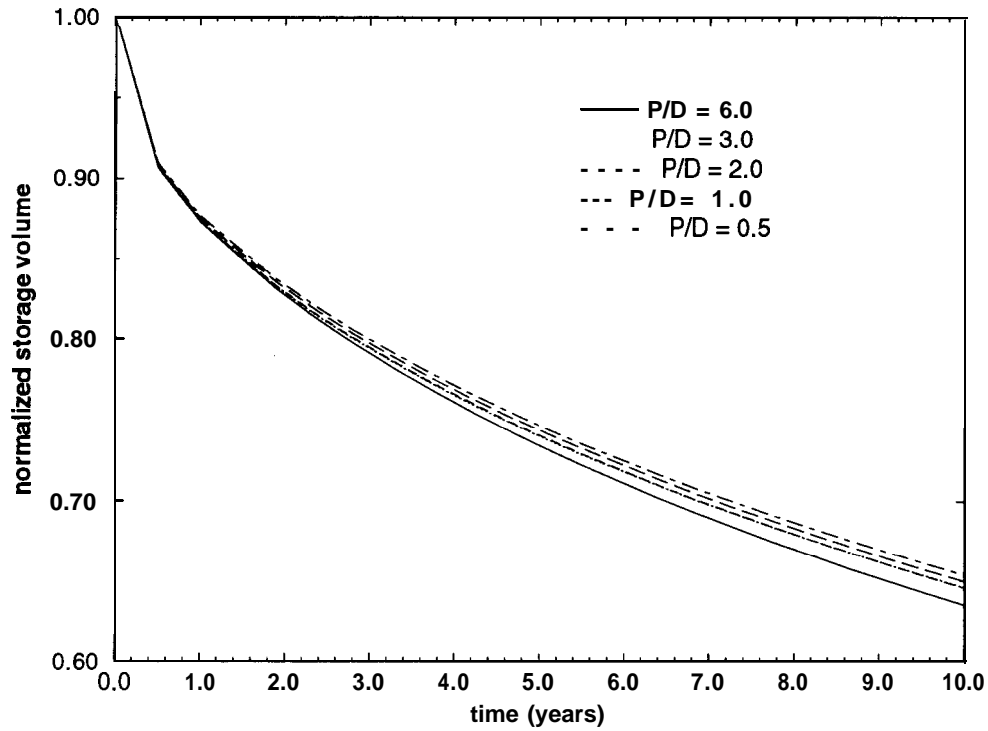


Figure 12. Normalized storage volume as a function of time for P/D ratios of 6.0, 3.0, 2.0, 1.0, and 0.5.

The normalized storage volume is plotted in Figure 12 as a function of time for all of the P/D ratios investigated. In each case the total facility storage volume is normalized with respect to the original volume. The plot shows that the storage volume history is characteristically the same for all of the P/D ratios studied. In addition, the plot shows that, as the P/D ratio is increased, the total facility storage loss increases. Again, this is probably due to the fact that for the larger P/D ratios there is more salt available (in the pillars) for creep.

3.3 Subsidence

The large displacements of the salt above and the horizontal movement of salt near the cavern array (as shown in Figure 7) results in surface subsidence. Figure 13 shows a magnified (1000x) deformed shape plot of the overburden and caprock layers. This plot is for a P/D = 3.0, but it is typical of all the geometries. The actual subsidence profiles at 10 years into the simulation are plotted in Figure 14 for the five P/D ratios and a single cavern with an equivalent volume of a seven cavern array. Within the range of P/D ratios examined in this study, subsidence troughs do not develop over the individual caverns (except for the case of P/D = ∞). One large trough is formed which extends approximately 10,000 ft from the center cavern, and the maximum subsidence occurs over the center cavern. Note that the extent of subsidence is beyond the “zone of influence,” a cone formed by a 45° angle from the deepest point of the cavern which has been hypothesized as the region of influence of a cavern array (stress changes, subsidence, etc.). The extent of subsidence does not change significantly for the various P/D ratios.

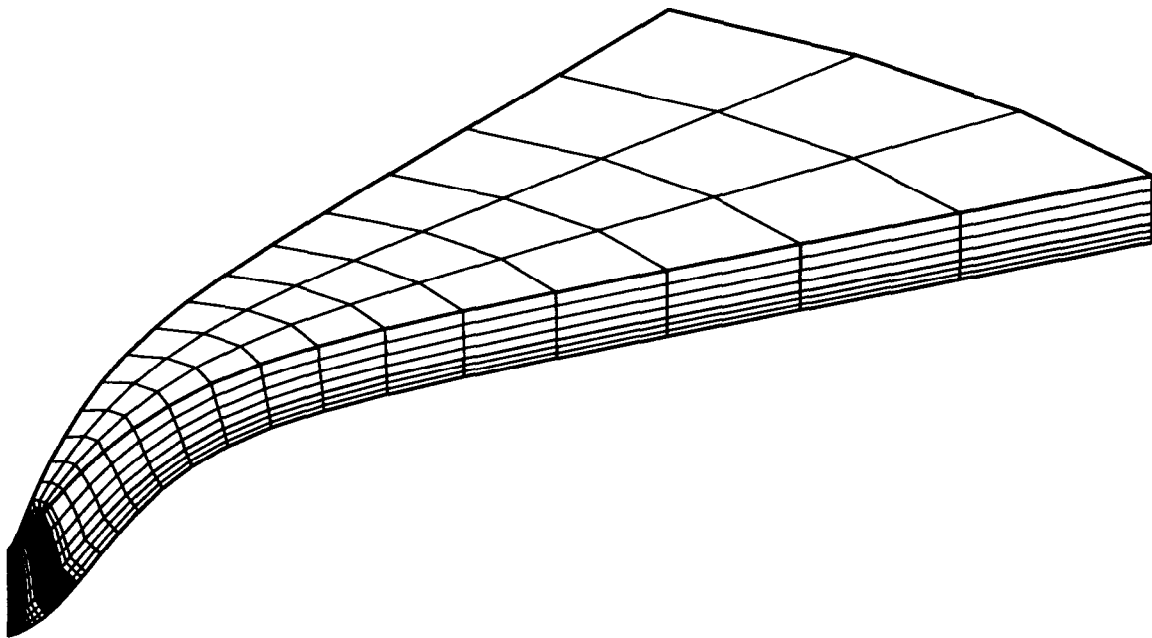


Figure 13. Magnified (1000 x) subsidence plot of caprock and overburden layers at 10 years.

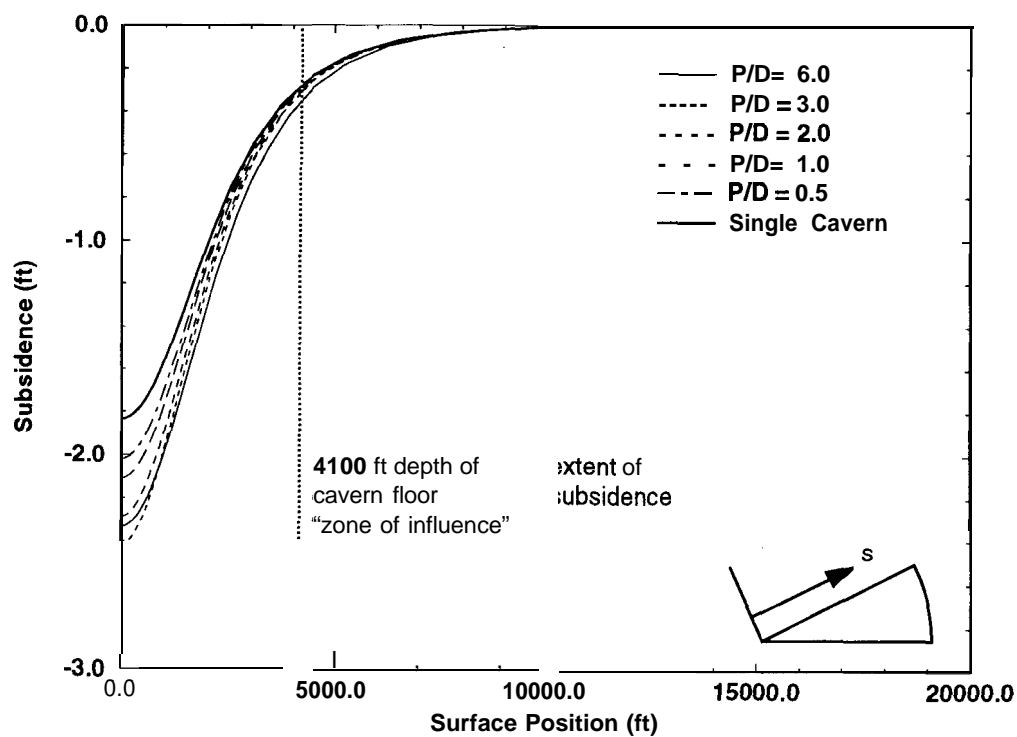


Figure 14. Subsidence profiles at 10 years for $P/D = 6.0, 3.0, 2.0, 1.0,$ and 0.5 and for a single cavern of equivalent volume ($P/D = 0.0$).

The subsidence over the center cavern at 10 years is plotted in Figure 15 as a function of P/D . The subsidence over the center cavern is a maximum for $P/D = 3.0$. As explained in the previous section, when the P/D is reduced, the storage loss decreases; thus, the subsidence magnitude decreases. As the P/D is increased above 3.0, the subsidence profile broadens, resulting in a smaller maximum subsidence. A single cavern calculation ($P/D = \infty$) yields a maximum subsidence of 0.17 ft.

The subsidence volume at 10 years is plotted in Figure 16 normalized to the original storage volume of the seven cavern array. Although the maximum subsidence decreases for $P/D > 3$, the broader subsidence profile observed in Figure 14 yields more subsidence volume.

3.4 Cavern Stability

The salt stability criterion is plotted in Figure 17 for $P/D = 6.0$ and 3.0 and in Figure 18 for $P/D = 2.0, 1.0$, and 0.5 at 10 years. The contours represent a factor of safety relative to the strain-to-rupture. According to the criterion, the lightest contour ($F \leq 1.0$) is the region where instability may occur. The remaining contours ($F > 1.0$), stability is assured. In all five cases the criterion indicates that salt fracture may occur along the lining at the lower half of the cavern.

Note that in the cases of $P/D = 1.0$ and 0.5, stability through the pillar cannot be guaranteed based on this criterion. Since this criterion is strain dependent, the other geometries may eventually exhibit through-pillar instability. Figure 19 is a plot of the stability function versus time for the five P/D ratios for a point located midway between the center and surrounding caverns, 500 ft from the cavern floor. For $P/D = 0.5$ and 1.0 the stability function is below or very near 1.0 at 10 years. Larger P/D ratios show a substantial increase in the stability function. For $P/D = 3.0$, the stability function has a value of 5.5 at 10 years and is leveling off such that through-pillar instability will not occur for a long time into the future.

As Equations (4) and (5) indicate, this criterion suggests that the creep-to-rupture increases with pressure up to a limit of 870 psi. Above 870 psi, the creep-to-rupture remains constant. Thus, based on this criterion, raising the operating pressure of the cavern will increase the strain-to-rupture and reduce the amount of creep experienced by the caverns. Since the operating pressures selected for this analysis are conservatively low, the results presented in this section represent a worst case.

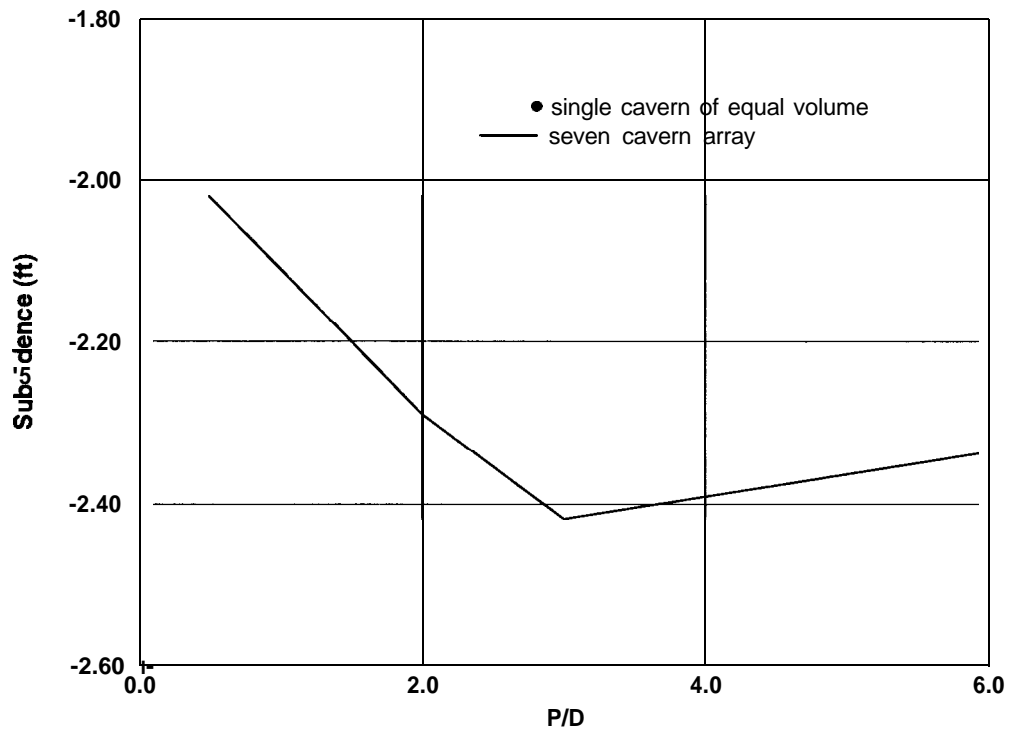


Figure 15. Subsidence over center cavern at 10 years as a function of P/D.

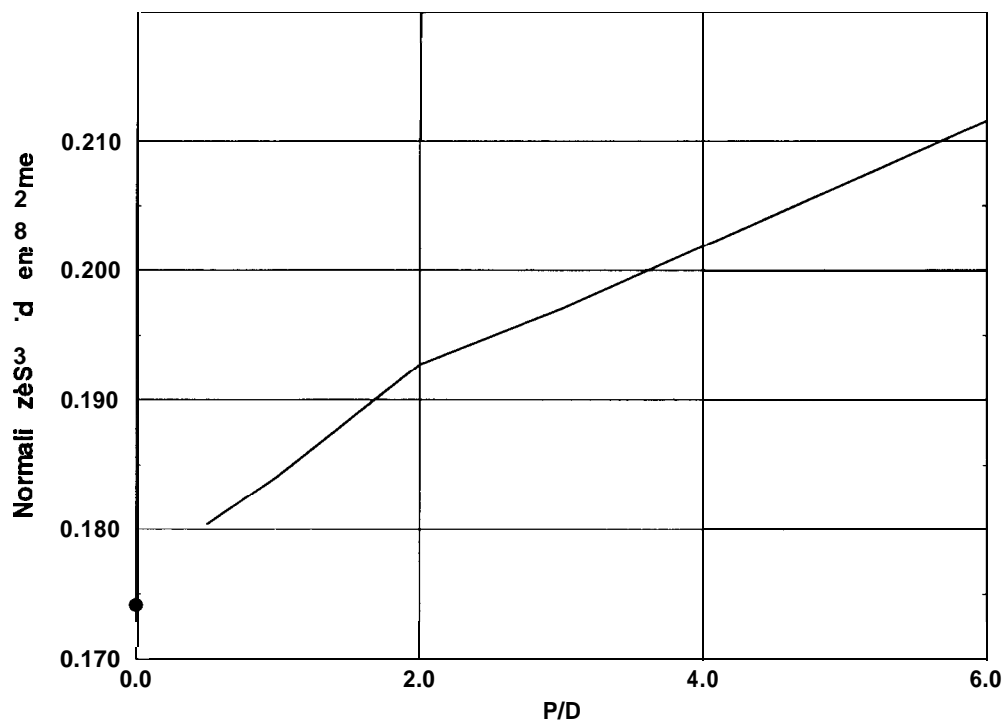


Figure 16. Subsidence volume at 10 years versus P/D. Subsidence volume is normalized by the original storage volume of the seven cavern array.

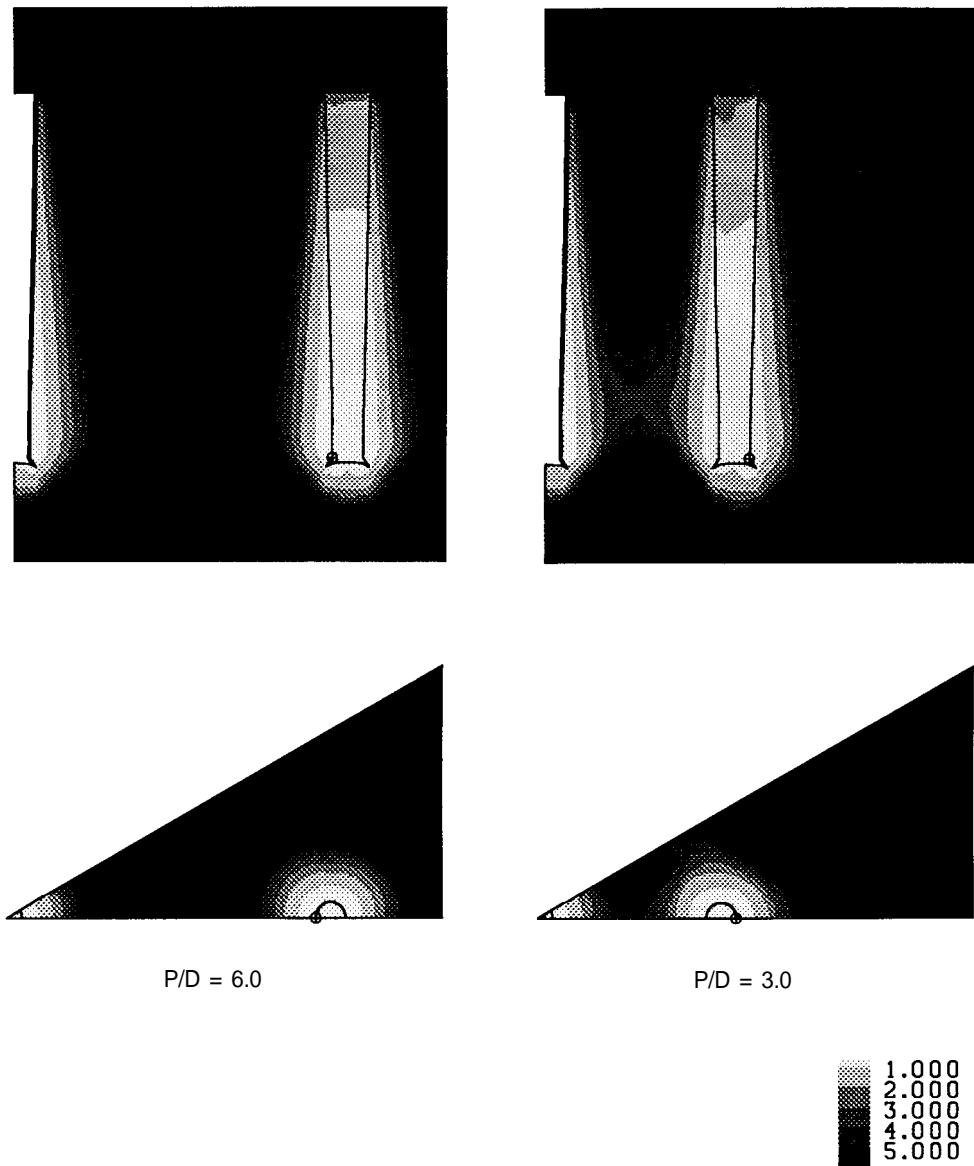


Figure 17. Creep rupture stability criterion (Equation (6)) for $P/D = 6.0$ and 3.0 at 10 years. Horizontal cross section taken approximately 500 ft from cavern floor.

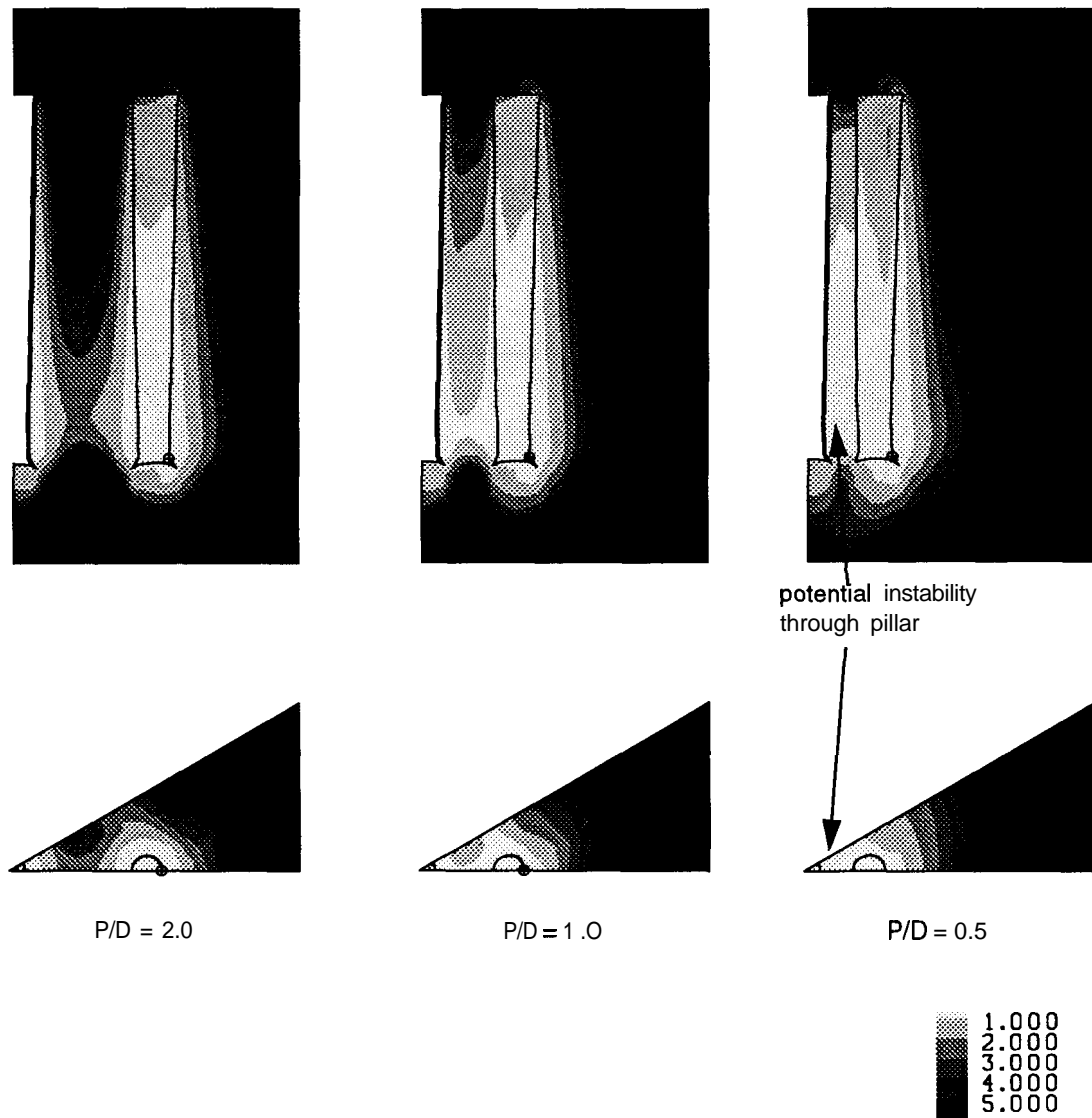


Figure 18. Creep rupture stability criterion (Equation (6)) for $P/D = 2.0$, 1.0 , and 0.5 at 10 years. Horizontal cross section taken approximately 500 ft from cavern floor.

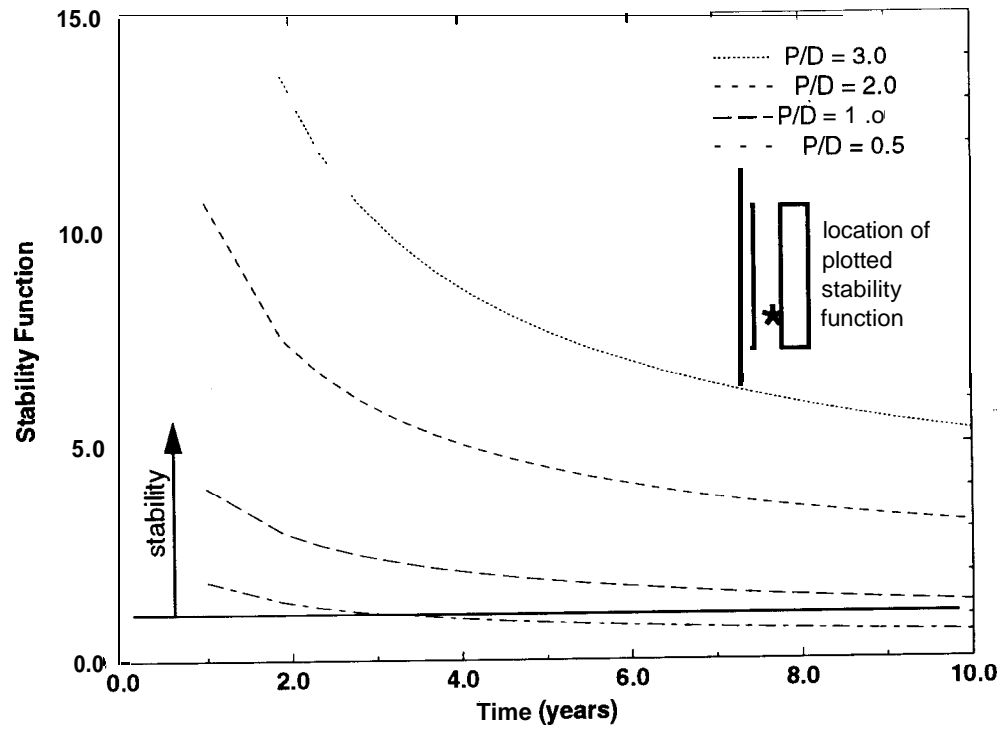


Figure 19. Stability function versus time for $P/D = 3.0$, 2.0 , 1.0 , and 0.5 .

4 Conclusions

A series of calculations were performed for gas-filled caverns in domal salt with P/D (pillar/diameter) ratios of ∞ , 6.0, 3.0, 2.0, 1.0, and 0.5. Based on the calculations presented in this memo, the following conclusions were made:

- With respect to cavern deformation, there is little difference between P/D ratios of 6.0, 3.0 and 2.0. Lower P/D ratios yielded nonsymmetric closure of the caverns.
- Storage volume is relatively insensitive to P/D ratio. However, a slight dependency on P/D ratio was exhibited in which the storage loss increased as P/D ratio increased. This behavior, though counter-intuitive, was due to there being more salt available between caverns with larger P/D ratios to displace storage volume.
- Subsidence profiles do not exhibit multiple troughs for the range of P/D ratios examined in this memo, but rather a single trough with a maximum subsidence over the center cavern. Subsidence volume increases with increasing P/D ratio over the range examined in this memo. The subsidence magnitude over the center cavern also increases with increasing P/D, up to P/D = 3.0. For P/D > 3.0, the maximum subsidence decreases and the subsidence trough broadens.
- The stability criterion indicated that through-pillar instability was possible for the cases of P/D = 0.5 and 1.0. Furthermore, the stability criterion indicated that failure was possible along the lining of the caverns for all the P/D ratios examined. However, this is not a prediction of failure since the criterion is conservative in that it can only predict stability. Furthermore, the load conditions represent a worst case operating history.
- In order to design cavern fields which optimize the use of available salt, a more rigorous criterion would be needed which could more accurately predict failure of rock salt. Using such a criterion, the allowable P/D could potentially be lower than indicated in these results.

5 References

- 1 J. H. Biffle, ***JAC3D - A Three-Dimensional Finite Element Computer Program for the Nonlinear Quasistatic Response of Solids with the Conjugate Gradient Method***, SAND87- 1305, Sandia National Laboratories, Albuquerque, New Mexico; In Preparation.
- 2 D. S. Preece and W. R. Wawersik, ***Leached Salt Cavern Design Using a Fracture Criterion for Rock Salt***, 25th Symposium on Rock Mechanics, Northwestern University, 1984.
- 3 E. L. Hoffman, ***Investigation of Analysis Assumptions for SPR Calculations***, memo to J. K. Linn, Sandia National Laboratories, Albuquerque, New Mexico, February 7, 1992.
- 4 R. S. Carmicheal, ***Handbook of Physical Properties of Rocks***, Vol. 2 of 3.
- 5 R. D. Krieg, ***Reference Stratigraphy and Rock Properties for the Waste Isolation Pilot Plant (WIPP) Project***, SAND83- 1908, Sandia National Laboratories, Albuquerque, NM, January 1984.
- 6 W. Herrmann and H. S. Lauson, ***Analysis of Creep Data for Various Natural Rock Salts***, SAND8 1-2567, Sandia National Laboratories, Albuquerque, NM, December 1981.
- 7 W. Herrmann and H. S. Lauson, ***Review and Comparison of Transient Creep Laws Used for Natural Rock Salt***, SAND8 1-0738, Sandia National Laboratories, Albuquerque, NM, April 198 1.
- 8 H. S. Morgan and R. D. Krieg, ***A Comparison of Unified Creep Plasticity and Conventional Creep Models for Rock Salt Based on Predictions of Creep Behavior Measured in Several In-Situ and Benchscale Experiments***, SAND87-1867, Albuquerque, NM, April, 1988.
- 9 H. S. Morgan and R. D. Krieg, ***Investigation of an Empirical Creep Law for Rock Salt that Uses Reduced Elastic Moduli***, Rock Mechanics Contributions and Challenges: Proceedings of the 31st U.S. Symposium, A.A. Balkema Publishers, Brookfield, VT, 1990, pp. 965-972.

Distribution

US DOE SPR PMO (5)
900 Commerce Road East
New Orleans, LA 70123
Attn: D. W. Whittington
R. Meyers, PR-622
L. Rousseau, FE-443
TDCS (2)

US DOE SPR (2)
1000 Independence Avenue SW
Washington, DC 20585
Attn: D. Johnson
D. Smith

Boeing Petroleum Services (3)
850 S. Clearview Parkway
New Orleans, LA 70 123
Attn: K. Wynn
T. Eyerman
K. Mills

Tejas Power Corporation (4)
14811 St. Mary's Lane
Suite 200
Houston, TX 77079
Attn: Greg Graves (3)
Jack Gatewood (1)

Technology Management (1)
48 Pulitzer Drive
Menlo Park, CA 94025
Attn: Milton Klein

1425 J. H. Biffle
1425 M. L. Blanford
1401 J. R. Asay
1434 D. R. Martinez
1501 C. W. Peterson
1561 H. S. Morgan
1561 E. L. Hoffman (6)
1561 C. M. Stone
1561 J. R. Weatherby
1562 R. K. Thomas
6101 P. J. Hommert
6112 D. A. Northrop
6112 D. S. Preece
6113 S. J. Bauer
6113 B. L. Ehgartner
6113 T. E. Hinkebein
6113 P. S. Kuhlman
6113 J. K. Linn
6113 R. V. Matalucci
6113 J. T. Neal
6113 J. L. Todd
6113 S. T. Wallace
6117 W. R. Wawersik
6121 D. E. Munson
6121 J. R. Tillerson
7141 Technical Library (5)
7151 Technical Publications
7613-2 Document Processing for DOE/
OSTI (10)
8523-2 Central Technical Files